RSC Sustainability

ROYAL SOCIETY OF CHEMISTRY

PAPER

View Article Online
View Journal | View Issue

Cite this: *RSC Sustainability*, 2025, **3**, 5518

Green synthesis of jarosite nanoparticles for photocatalytic degradation of Rhodamine B under simulated sunlight radiation

Hui Wen Neo,[a] Eslam M. Hamed,[ab] Fun Man Fung *[cd] and Sam F. Y. Li *[a]

Green synthesis of efficient photocatalysts using agricultural waste is a promising approach toward sustainable wastewater treatment. In this work, magnetite (Fe_3O_4) and jarosite ($KFe_3(SO_4)_2(OH)_6$) nanoparticles were synthesized using banana peel extract as a natural reducing/stabilizing agent and potassium source under microwave-assisted conditions. The structural, optical, and magnetic properties of the nanoparticles were systematically characterized. Photocatalytic performance was evaluated for Rhodamine B (RhB) degradation under simulated sunlight irradiation, and reaction kinetics were analyzed using pseudo-first-order models. Jarosite exhibited a rate constant (k) of 0.0198 min^{-1}, approximately double that of magnetite (k = 0.0098 min^{-1}), achieving >99% RhB removal within 30 minutes. Mechanistic studies, including scavenger tests and photoluminescence analysis, confirmed the dominant role of $^{\bullet}OH$ radicals and efficient charge separation in jarosite. The catalyst retained >94% activity over five cycles, and total organic carbon (TOC) removal reached 92%, indicating effective mineralization. This study demonstrates a low-cost, scalable, and environmentally friendly route for synthesizing iron-based photocatalysts, aligning with the UN Sustainable Development Goals (SDGs) for clean water and responsible consumption.

Received 6th September 2025
Accepted 10th October 2025

DOI: 10.1039/d5su00731c

rsc.li/rscsus

Sustainability spotlight

Global wastewater pollution from industrial dyes poses a severe threat to both ecosystems and human health. Conventional treatment methods are often inefficient, costly, and resource-intensive. This work addresses this critical issue by developing a green, cost-effective, and highly efficient method for wastewater remediation. We achieved this by synthesizing iron-based photocatalysts, specifically jarosite nanoparticles, from agricultural waste—banana peels—which serve as a natural stabilizing agent and a source of potassium. This approach significantly reduces the need for hazardous chemicals and minimizes waste generation. The resulting jarosite nanoparticles demonstrated superior photocatalytic activity, achieving a remarkable 99.1% degradation of the organic dye Rhodamine B, outperforming a conventional iron-based catalyst (magnetite) and maintaining high efficiency over multiple uses. This study provides a novel and sustainable solution for water purification. This work directly aligns with Clean Water and Sanitation (SDG 6), by improving water quality and substantially increasing recycling and safe reuse. It also contributes to Responsible Consumption and Production (SDG 12), by reducing waste generation through the use of an agricultural byproduct as a valuable resource and promoting efficient use of natural resources. Finally, it supports Industry, Innovation, and Infrastructure (SDG 9), as it introduces a new and sustainable industrial process for producing advanced materials for environmental remediation.

Introduction

The increasing contamination of wastewater with numerous pollutants, including heavy metals, organic compounds, and dyes, poses a significant environmental threat. Globally, over 700 000 tons of synthetic dyes are discharged annually into aquatic systems, posing serious risks to ecosystems and human health. Conventional wastewater treatment methods usually struggle to eliminate these contaminants effectively, releasing them into the environment. Nanoparticles, particularly metal and metal oxide nanoparticles, have emerged as promising alternatives for wastewater treatment because of the unique physicochemical characteristics, such as large surface areas, high reactivity, and tuneable morphology.[1–3] In particular, iron-based nanoparticles are known to effectively remove a wide range of pollutants *via* adsorption and have the potential to degrade contaminants through Fenton-like reactions or photocatalysis.[4–6]

However, conventional synthesis methods for iron-based nanoparticles often involve hazardous chemicals and operating conditions with a considerable environmental impact, such as high temperature, vacuum conditions, or inert

[a]*Department of Chemistry, Faculty of Science, National University of Singapore, 3 Science Drive 3, Singapore, 117543, Singapore. E-mail: chmlifys@nus.edu.sg*
[b]*Department of Chemistry, Faculty of Science, Ain Shams University, Abbassia, Cairo, 11566, Egypt*
[c]*School of Chemistry, University College Dublin, Belfield, Dublin 4, D04 C1P1, Ireland. E-mail: funman.fung@ucd.ie*
[d]*UCD Geary Institute for Public Policy, University College Dublin, Belfield, Dublin D04 N9Y1, Ireland*

atmospheres.[7–9] Green synthesis provides a sustainable and eco-friendly method for nanoparticles synthesis by employing plant extracts, microorganisms, and other natural sources as reducing and stabilizing agents,[10] and replacing organic solvents with water as the medium for synthesis, reducing the production of harmful byproducts and disposal of organic waste.[11,12] The use of biomass waste can further align with the principles of green chemistry, where the use of renewable feedstock is increased, and the waste generated is further decreased.[13] One such example is banana peels, a common household and commercial waste. Banana peels are rich in antioxidants, containing a diverse range of polyphenols such as flavonoids, terpenoids, and carotenoids that can be extracted,[14] making them a viable green alternative for the synthesis of iron-based nanoparticles.

A promising field of iron-based nanoparticles for wastewater treatment involves magnetic iron oxide nanoparticles such as magnetite (Fe_3O_4). Magnetite nanoparticles exhibit superparamagnetism, and this unique magnetic property allows for effective recovery of the nanoparticles, mitigating the issue of nano-contamination and reducing recovery costs.[15,16] The low cost, natural prevalence, and superparamagnetic characteristics have led to extensive studies into their synthesis and application in wastewater treatment.[17–21] Existing literature has succeeded in synthesizing iron oxide nanoparticles, specifically magnetite and maghemite, using banana peel extracts,[22,23] but their applications in wastewater treatment have yet to be evaluated. Magnetite has also been extensively studied as an adsorbent for heavy metals or organic contaminants, but its role as a photocatalyst has rarely been reported.[17]

Another potential iron-based nanoparticle is jarosite, a form of iron-based hydroxysulphate mineral with the formula $KFe_3(SO_4)_2(OH)_6$.[24,25] Jarosites are good scavengers for certain metals and are applied at the industrial scale, mainly to remove iron in the zinc hydrometallurgy process.[26] Lab-scale studies have revealed potential applications in other fields for its adsorption and catalytic performance,[27] such as its ability to photocatalytically degrade organic pollutants in wastewater, such as sulfamethoxazole[28] and Congo red.[29] Jarosite is commonly synthesized by chemical or biological methods. In chemical synthesis, a potassium precursor such as KNO_3 or K_2SO_4 is heated with iron(III) sulphate under acidic conditions.[30]

On the other hand, biological synthesis mimics the natural formation mechanism of jarosite involving microbiological oxidation of ferrous sulphate.[28,30] The high potassium content found in the banana peel extract indicates its great potential to be utilized in the green synthesis of jarosite.[31] Unlike magnetite, which requires sodium hydroxide for the co-precipitation process, jarosite was synthesized using only the iron precursor and the banana peel extract, which makes the method more environmentally friendly and enhances the photocatalytic activity.

Despite the well-documented use of magnetite in environmental remediation, jarosite has received comparatively little attention as a photocatalyst, particularly when synthesized through green methods. While previous studies have investigated jarosite for metal adsorption or as a byproduct in hydrometallurgical processes, its band structure, stability, and potential for reactive oxygen species (ROS) generation make it a promising candidate for dye degradation. However, traditional synthesis methods for jarosite often rely on high temperatures, acidic media, and synthetic potassium sources, which contradict the principles of green chemistry. As far as we are concerned, this study is among the first to utilize banana peel extract as a natural potassium source in addition to its function as a reducing and stabilizing agent for the green synthesis of jarosite nanoparticles. This strategy reduces chemical inputs and leverages agricultural waste, offering a dual benefit of pollutant remediation and waste valorisation. Moreover, a direct performance comparison between green-synthesized magnetite and jarosite in photocatalytic dye degradation under simulated sunlight has not been thoroughly explored in prior literature.

Rhodamine B (RhB) is usually used as a model organic pollutant because it is a widely produced water-soluble dye used in textile and related industries, has a strong, well-characterized visible absorption band ($\lambda_{max} \approx 554$ nm) which makes quantitative monitoring straightforward, and is known to exhibit acute ecotoxicity in aquatic organisms. These properties make RhB a convenient and reproducible probe to benchmark photocatalytic activity and reaction kinetics under simulated sunlight.

In addition to photocatalysis, several advanced oxidation processes (AOPs) have been explored for the degradation of RhB and other persistent dyes.[32,33] These include heterogeneous Fenton and photo-Fenton processes using Fe^{2+}/Fe^{3+} catalysts activated by H_2O_2 under UV or visible light,[34] as well as persulphate-based systems where $SO_4^{\bullet-}$ radicals are generated thermally, photochemically, or *via* transition metal activation.[35] Catalysts such as doped TiO_2, ZnO, MnO_2, and various Fe-based composites have been reported to significantly enhance RhB degradation rates by promoting ROS formation. Coupled processes, such as photo-Fenton combined with ultrasound or electrochemical activation, have also shown synergistic effects in accelerating mineralization.[36] These studies highlight the importance of designing catalysts that enable efficient ROS generation under solar irradiation, providing motivation for the development of sustainable photocatalysts like magnetite and jarosite synthesized *via* green routes.

Herein, jarosite nanoparticles were greenly synthesized in a microwave oven using banana peel extract as a stabilizing agent and a source of potassium. The photocatalytic activity was assessed in the degradation of RhB in wastewater. Magnetite nanoparticles were also synthesized and evaluated for comparative study. This study aims to develop a green synthesis method for jarosite and magnetite nanoparticles using banana peel extract and to comparatively assess their photocatalytic performance in RhB degradation under simulated sunlight; a technique that could pave the route for future studies on the scalability of the green synthesis of jarosite and its application in the photocatalytic degradation of persistent organic pollutants.

Materials and methods

Chemicals

Iron(II) sulphate heptahydrate ($FeSO_4 \cdot 7H_2O$) was purchased from Merck. Iron(III) sulphate ($Fe_2(SO_4)_3$) was purchased from Riedel-de Haën. RhB, isopropyl alcohol (IPA), *p*-benzoquinone (PBQ), and

ethylenediaminetetraacetic acid (EDTA) were purchased from Sigma-Aldrich. Hydrogen peroxide (30% w/w) was purchased from Scharlau. The chemicals were used without further purification. Bananas were purchased from a local supermarket (FairPrice) and then the peels were collected for extraction.

Banana peel extract

The banana peels were cleaned, sliced into tiny pieces, and left in the oven for 3 days at 80 °C to dry them out (Fig. S1). 4 g of the dried banana peels were added to 40 mL of deionized water, then heated under reflux for 10 minutes in a microwave with an output power of 650 W at 100% power. The resulting solution was filtered with a syringe attached to a 0.45 μm hydrophilic polytetrafluoroethylene (PTFE) filter, and the filtrate was stored at 4 °C for later use.

Magnetite synthesis

$FeSO_4 \cdot 7H_2O$ (0.2 M) and $Fe_2(SO_4)_3 \cdot xH_2O$ (0.2 M) were mixed in a 2 : 3 ratio. The solution was heated to 60 °C for 5 minutes under continuous stirring at 500 rpm, then 1 M NaOH was added dropwise to the solution until pH was adjusted to 11, followed by the addition of the banana peel extract. The formed precipitate was collected with a magnet and washed with deionized water for multiple cycles until the supernatant reached pH 7. The residue was then collected and dried overnight in an oven at 80 °C. The dry residue was ground to a fine powder before being stored in glass vials. Optimization studies were carried out by varying NaOH addition rate (pH 10–12) and banana extract volume (5–20 mL). A pH = 11 and 10 mL extract yielded magnetite with highest crystallinity and photocatalytic activity. The synthesis process of magnetite is illustrated in Fig. S2.

Jarosite synthesis

$Fe_2(SO_4)_3 \cdot xH_2O$ (0.2 M) and banana peel extract were mixed in a 1 : 1 volume ratio. The solution was heated under reflux for 30 minutes in a microwave oven with an output power of 650 W at 100%. The resulting precipitate was washed and centrifuged until the supernatant had a pH of 7. The residue was collected, dried in an oven at 80 °C, and ground to a fine powder before storage. The synthesis process of jarosite is illustrated in Fig. S3.

Optimization was conducted by adjusting the iron-to-banana ratio and the duration of heating in the microwave. The ratio of iron to banana in the mixture was adjusted by preparing separate banana extracts where dried banana peels were added to deionized water in a 1 : 10 and 1 : 20 ratio. The duration of heating the iron–banana mixture in the microwave varied between 10 to 30 minutes in intervals of 10 minutes. Optimization was carried out by conducting triplicates of degradation experiments using 0.5 mg mL^{-1} catalyst and 5% H_2O_2 under simulated sunlight irradiance for 10 minutes. The synthesis procedure was repeated three times with banana peels from different sources. The iron concentration in the final product varied by less than 2%, confirming reproducibility.

Characterization

X-ray diffraction (XRD) was carried out at room temperature for a continuous scan of 2θ from 20° to 80° using a Bruker D8 Advance Powder X-ray Diffractometer with Cu K_α radiation (λ = 1.5418 Å). Scanning electron microscopy (SEM) images were obtained using the JEOL JSM-6701F Field Emission Scanning Electron Microscope as a 30 kV class analytical SEM. Particle size distributions were obtained from high-magnification SEM micrographs using ImageJ (Fiji) software. For each sample, multiple representative images (3–5) at the same magnification were analysed. The SEM scale bar was used to set the image scale; particles were segmented by thresholding and particle outlines were measured using the Feret diameter (maximum caliper). At least 100 particles were measured per sample (N = 112 for magnetite; N = 128 for jarosite). The mean particle size and standard deviation were calculated and reported as mean ± SD. Fourier-transform infrared (FTIR) spectra of the synthesized materials (Fig. S5) show distinct vibrational signatures consistent with magnetite and jarosite structures. Jarosite exhibits strong sulphate stretching bands in the 1150–1000 $^{-1}$ region (ν_3 and ν_1/ν_2 modes of SO_4^{2-}), together with a broad O–H stretching envelope cantered around 3400 cm^{-1} arising from structural OH groups and adsorbed water. On the other hand, magnetite is characterized by intense Fe–O lattice bands in the 600–500 cm^{-1} region (typical Fe–O stretching modes), while only weak O–H related features are observed, indicating lower surface hydroxylation relative to jarosite. An Agilent Cary 60 UV/Vis spectrophotometer was used for all absorbance measurements. Diffused reflectance spectra (DRS) were carried out using UV-2600i UV-Vis Spectrometer with an Integrating Sphere. Photoluminescence measurements were performed on a Horiba Fluorolog-3 spectrofluorometer. EZ9 MicroSense Vibrating Sample Magnetometer (VSM) was used to measure the magnetic hysteresis loop at room temperature and a typical magnetic field of 1.5 Tesla. AULIGHT Xenon Lamp System (CEL-S500) of optical power 1 Sun (=100 mW cm^{-2}) was used as the simulated sunlight source for the degradation experiments.

Degradation experiments

To study the effectiveness of the catalyst in the degradation of RhB, differing concentrations of H_2O_2 and different amounts of the catalyst were added to 5 mg L^{-1} of RhB solution. The solution was left under simulated sunlight irradiance for different durations. Radical scavenging experiments were also conducted by adding 1% IPA, 1 mM PBQ, and 1 mM EDTA separately to capture hydroxyl radicals, superoxide radicals, and photogenerated holes, respectively.[37] The difference in the absorbance of RhB between the beginning and the end of the experiments was determined using the UV-Vis spectrophotometer at λ_{max} = 554 nm. The presence of H_2O_2 classifies the process as a photo-Fenton-like AOP.

Results and discussion

Structural analysis

X-ray diffraction (XRD) was used to determine the phase of the synthesized iron-based nanoparticles. The peaks in Fig. 1A are found at 2θ = 30.1°, 35.3°, 43.1°, 53.5°, 57.2°, and 63.0°, which match the (220), (311), (400), (422), (511) and (440) planes of

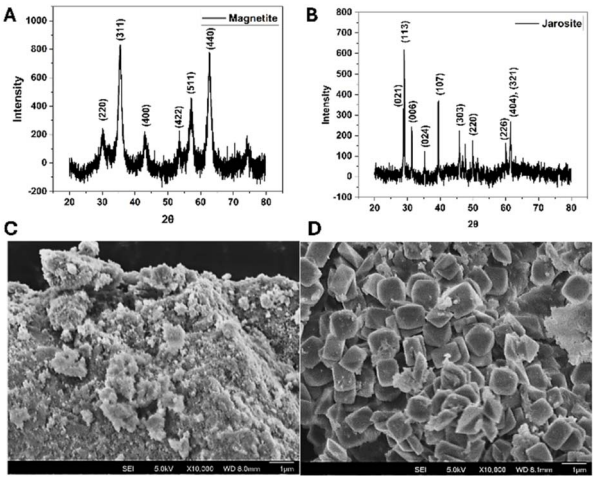

Fig. 1 XRD patterns of the greenly synthesized (A) magnetite and (B) jarosite. Scanning Electron Microscopy (SEM) images of the greenly synthesized (C) magnetite and (D) jarosite. Scale bar: 1 μm.

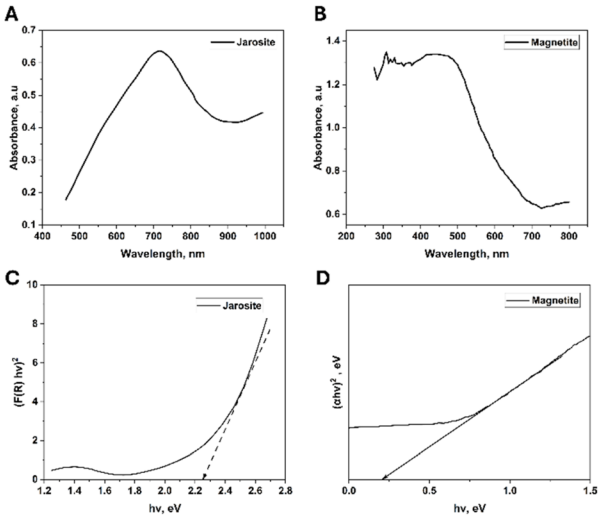

Fig. 2 UV-Vis diffuse reflectance spectra of (A) jarosite and (B) magnetite. (C) Kubelka–Munk plot of jarosite and (D) Tauc plot of magnetite.

magnetite.[22] The XRD pattern in Fig. 1B shows peaks at 2θ = 28.7°, 29.0°, 31.3°, 35.3°, 39.4°, 45.8°, 49.8°, 60.0°, and 61.4°, which correspond to the (021), (113), (006), (024), (107), (303), (220), (226), and (404), (321) planes of the jarosite crystal.[38]

SEM imaging was performed to confirm that the two synthesis routes produced morphologically distinct nanoparticles. The SEM images obtained for magnetite and jarosite are shown in Fig. 1C and D and S4. The SEM image of jarosite shows clear cubic structures, whereas the SEM image of magnetite shows an agglomerated surface without the uniform crystal structures observed in jarosite. From SEM image analysis, the magnetite nanoparticles showed an average Feret diameter of 45 ± 10 nm. Jarosite particles exhibited a smaller average particle size of 25 ± 5 nm. XRD Scherrer analysis $\left(D = \frac{K\lambda}{\beta\cos\theta}\right)$ yielded crystallite sizes of ~40 nm for magnetite and ~15 nm for jarosite. Where D = crystallite size, $K \approx 0.9$ (shape factor), λ = X-ray wavelength (Cu Kα = 0.15418 nm), β = full width at half maximum in radians (instrument-broadening corrected), and θ = Bragg angle.

Optical properties

UV-Vis Diffuse reflectance spectroscopy (DRS) was utilized to analyse the optical properties of jarosite and magnetite as shown in Fig. 2A and B. The small band gap of magnetite resulted in a wide band in the visible and UV regions. Whereas, in the case of jarosite, a peak was observed at 710 nm with a more significant visible light absorption.

The optical band gap (E_g) of jarosite was estimated using the Kubelka–Munk function, $F(R)=(1-R)^2/2R$, which converts diffuse reflectance data into a pseudo-absorption coefficient suitable for powdered samples.[39] The plot of $[F(R)h\nu]^{1/2}$ *versus* $h\nu$ was extrapolated to obtain the bandgap energies. On the other side, the magnetite sample had strong specular reflection, K–M failed and gave misleading $F(R)$. Therefore, the Tauc method was adopted for magnetite colloidal suspension using the equation $(\alpha h\nu)^2 = A(h\nu - E_g)$, where α is the coefficient to absorption, $h\nu$ is the photon's energy, A is the constant, and E_g is the direct bandgap (eV). The Kubelka–Munk and Tauc plots of jarosite and magnetite are shown in Fig. 2C and D. The figures show that jarosite exhibited a band gap of 2.25 eV, while magnetite exhibited a narrow band gap of 0.24 eV, confirming its strong absorption in the visible region. The low band gap of magnetite indicates that it is devoid of maghemite (γ-Fe_2O_3) contamination, oxidation effects, or indirect band transitions. The photocatalytic properties of jarosite and magnetite are summarized in table S1.

Magnetic properties

To investigate the magnetic properties of the synthesized samples, magnetization measurements were conducted with a Vibrating Sample Magnetometer (VSM) at room temperature. The magnetic hysteresis loops (M–H) of jarosite and magnetite are presented in Fig. 3A and B, respectively. The as-synthesized magnetite exhibited superparamagnetic behaviour with a saturation magnetization (M_s) of 61.87 emu g^{-1}. Additionally, the coercivity (H_c) was found to be 35.12 Oe, indicating its soft magnetic nature.

On the other hand, jarosite displayed weak magnetic behaviour due to its antiferromagnetic nature, with a significantly lower M_s of 3.71 emu g^{-1} and higher H_c of 345.13 due to stronger magnetic anisotropy and antiferromagnetic interactions. The presence of iron in jarosite contributes to its magnetic response, but due to its structural arrangement and interactions, its magnetization is much lower compared to magnetite. These findings confirm the distinct magnetic characteristics of magnetite and jarosite, with magnetite demonstrating strong superparamagnetic properties and jarosite exhibiting weak magnetism.

Optimization of jarosite synthesis

The ratio of iron to banana present in the mixture was varied by adjusting the ratio of banana peels to deionized water used in

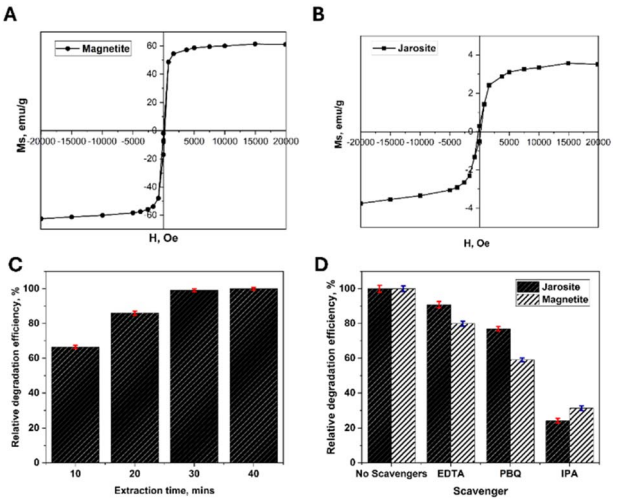

Fig. 3 M–H loop of as synthesized (A) magnetite and (B) jarosite. (C) Comparison of degradation efficiency of jarosite synthesized by different microwave heating intervals. (D) Removal efficiency of 5 mg L^{-1} RhB using 1 mg mL^{-1} magnetite and 0.5 mg mL^{-1} jarosite in the presence of different radical scavengers.

the preparation of the banana extract. Fig. S6 demonstrates that a banana extract prepared using a 1 : 20 (w/v) ratio effectively enabled the synthesis of jarosite with the highest degradation efficiency towards RhB. Beyond a 1 : 20 ratio, there was a decrease in the yield of jarosite, suggesting that potassium concentration in the banana extract was too low for the synthesis. When a 1 : 5 ratio was used, there was insufficient liquid to obtain the extract. Hence, in addition to the degradation efficiency of the synthesized jarosite, the lack of liquid at low ratio, and the dilution of the extract at higher ratios led to the adoption of a 1 : 20 as the optimum ratio for banana extract preparation.

Based on this, jarosite was then synthesized using banana extracts prepared in a 1 : 20 solid to liquid ratio. The mixture was heated in microwave under reflux for 10, 20, 30, and 40 minutes to determine the effect of duration of heating on the degradation efficiency of synthesized jarosite. As shown in Fig. 3C, jarosite synthesized by heating for 30 minutes exhibited the best photocatalytic degradation. Longer heating time didn't lead to any further enhancement in the degradation efficiency.

Photocatalytic degradation of Rhodamine B

Radical scavenging experiments were carried out using IPA, PBQ, and EDTA as scavengers for hydroxyl radicals, superoxide radicals, and photogenerated holes, respectively. As shown in Fig. 3D, the highest suppression occurs when 1% IPA is added, with a 68.8% and 75.9% suppression in the relative degradation efficiency of RhB for magnetite and jarosite, respectively.

The relative contributions of different ROS to the degradation process can be quantified based on the inhibitory effects observed upon the addition of specific scavengers. For jarosite, the presence of EDTA, PBQ, and IPA reduces the degradation efficiency from 100% (control) to around 90%, 75%, and 25%, respectively, indicating that holes, superoxide radicals, and hydroxyl radicals contribute about 10%, 25%, and 75% to the observed activity. In comparison, magnetite exhibits a decrease from about 100% to 80% with EDTA, 60% with PBQ, and 35% with IPA, respectively, highlighting relative contributions of 20% for holes, 40% for superoxide, and 65% for hydroxyl radical. The significant suppression in removal efficiency of RhB under the presence of IPA confirms that hydroxyl radicals are the predominant ROS. Hence, it is likely that magnetite and jarosite serve as photocatalysts for the homolytic cleavage of H_2O_2 to form hydroxyl radicals that would then react with RhB molecules, resulting in degradation of the organic dye.

Degradation performance of photocatalysts

The synthesized magnetite achieved 87.6% degradation of 5 mg L^{-1} RhB after 60 minutes of simulated sunlight irradiance. In comparison, jarosite was able to achieve 99.1% degradation of 5 mg L^{-1} RhB after 30 minutes of sunlight irradiance, and nearly 100% degradation after one hour (Fig. 4A and B).

Additionally, first-order kinetic plots were investigated for RhB degradation. The pseudo-1st-order kinetic standard was used to fit the photodegradation of RhB using the equation $\ln(C_t/C_0) = k_t$ where C_0/C_1 are the initial concentrations of pollutants, k is the rate constant, and t represents the reaction time (Fig. 4C).

Investigations into the catalyst's dosage effect were carried out as shown in Fig. 4D. Increasing jarosite concentration initially improved photocatalytic activity. This is explained by more readily available active sites for the processes of adsorption and photodegradation. However, the degradation efficiency decreased when the concentration was increased over 0.5 mg mL^{-1}. This might be the result of less light penetration into the system and poorer catalyst dispersion at elevated concentrations. Thus, a dosage of 0.5 mg mL^{-1} was adopted in all experiments.

Total organic carbon (TOC) analysis was performed to evaluate the extent of mineralization of RhB during photocatalytic

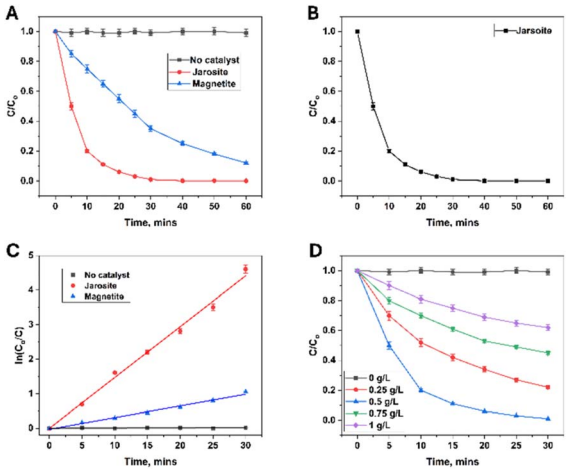

Fig. 4 (A and B) Photodegradation plots of RhB, (C) reaction kinetic plots, and (D) effect of jarosite concentration on RhB photodegradation.

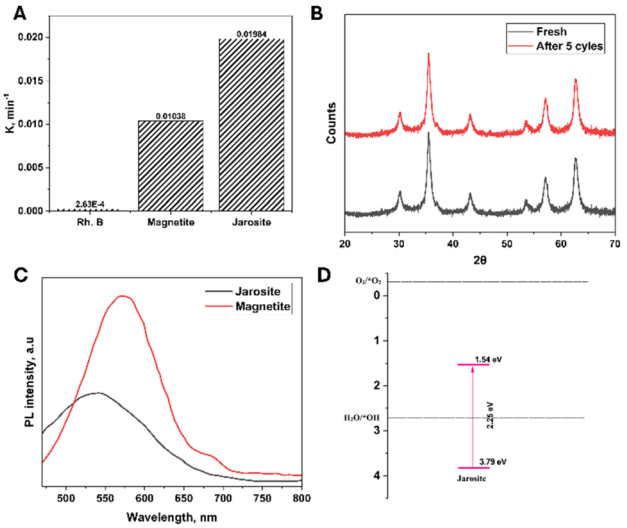

Fig. 5 (A) Pseudo-1st-order rate constants of the photocatalysts. (B) XRD patterns of jarosite before and after 5 cycles of the photocatalytic reaction. (C) Photoluminescence spectra of jarosite (black line) and magnetite (red line). (D) Energy band positions of jarosite.

treatment.[40] The jarosite catalyst achieved ~92% TOC removal after 60 min of irradiation, indicating near-complete mineralization of the dye into CO_2 and H_2O rather than partial degradation into intermediate by-products. In contrast, magnetite exhibited a slower mineralization rate, achieving approximately 63% TOC removal under identical conditions, which is consistent with its lower pseudo-first-order rate constant and slower decolorization kinetics. These results confirm that jarosite accelerates RhB degradation and ensures effective mineralization, which is a critical factor for environmentally safe wastewater treatment (Fig. S7).

The rate constant of RhB photodegradation for magnetite and jarosite is shown in Fig. 5a. Jarosite exhibited a maximum rate constant (0.0198 min^{-1}), which is about 2 times greater than magnetite. A comparison of RhB degradation between magnetite and jarosite with other iron-based photocatalysts is in Table 1.

Furthermore, the degradation activity was performed to evaluate the ability of the jarosite to maintain its photocatalytic activity after multiple cycles. Tested up to 5 cycles, jarosite maintained more than 94% of its catalytic activity. As shown in Fig. 5b, XRD patterns of jarosite after the 5th cycle showed no significant change in the characteristic peaks compared to the fresh one, confirming its great structural stability.

Photocatalytic mechanism

A study using photoluminescence (PL) spectroscopy was conducted to assess the synthesised photocatalysts' ability to separate and recombine photogenerated electron–hole (e–h) pairs. The electron–hole recombination rate directly correlates with PL intensity, where a higher PL intensity indicates a higher recombination rate of photogenerated carriers and a lower photocatalytic performance[41]

The PL profiles of magnetite and jarosite-based photocatalysts were examined at an excitation wavelength (λ_{exc}) of 320 nm, as shown in Fig. 5C. The magnetite sample exhibited higher PL intensity, suggesting that photogenerated electron–hole pairs recombined rapidly, leading to inefficient charge separation and lower photocatalytic activity. In contrast, in case of jarosite, a marked decrease in PL peak intensity was noticed. This reduction in PL intensity indicated a suppression of charge carrier recombination, which can be attributed to the effective trapping of photogenerated electrons by jarosite, enhancing charge transfer and mobility.

The valence band energy (EVB) and conduction band energy (ECB) potentials of magnetite and jarosite were calculated based on the following equations:[46]

$$E_{VB} = \chi - E_e + 0.5E_g$$

$$E_{CB} = E_{VB} - E_g$$

The VB and CB positions of jarosite were determined to be 3.79 eV and 1.54 eV, respectively, as shown in Fig. 5D. The CB potentials is more positive than the redox potential of $O_2/^{\bullet}O_2$ (−0.33 eV *vs.* NHE), indicating that direct reduction of O_2 into $^{\bullet}O_2$ by photogenerated electrons is not favourable. This suggests that alternative pathways or mediator species may be involved in the photocatalytic degradation.

However, the VB potential is significantly higher than the redox potential of $H_2O/^{\bullet}OH$ (2.72 eV *vs.* NHE), suggesting the photogenerated holes in jarosite possess strong oxidative power, enabling the efficient oxidation of H_2O into $^{\bullet}OH$ radicals. This aligns with the results of scavenger tests, confirming

Table 1 Comparison of different iron-based photocatalysts for the degradation of Rhodamine B

Catalyst	[Catalyst] (mg mL^{-1})	[RhB] (mg L^{-1})	[H_2O_2] (%)	Time (min)	Light	Degradation (%)	Ref.
Magnetite	1.5	13	2.7	60	UV light	99.5	37
Magnetite	0.51	5	0.068	120	Visible light	97.7	42
Magnetite	0.51	5	0.068	120	Sunlight	41.4	42
V–Ti magnetite/quartz	3.4	5	—	20	Simulated sunlight	98.0	43
Magnetite	~1	10	0.6	30	Visible light	97.5	44
Magnetite	5	10	—	180	Visible light	61.5	45
Magnetite	1	5	10	60	Simulated sunlight	87.6	This work
Jarosite	0.5	5	5	30	Simulated sunlight	99.1	This work

that ˙OH radicals play a dominant role in the photocatalytic mechanism of jarosite.

While magnetite has a lower band gap and absorbs more light, its rapid charge recombination, limited surface reactivity, and lower stability in aqueous environments make it less effective for photocatalysis compared to jarosite. Jarosite's wider band gap, slower recombination, versatile surface chemistry, and stability contribute to its superior photocatalytic activity.

A proposed mechanism for the enhanced activity of jarosite is summarized in Fig. 6 and is as follows:

Under simulated sunlight irradiation, jarosite absorbs incident photons, leading to the generation of photoexcited electron–hole pairs as described in eqn (1). The photogenerated holes in the valence band (VB) of jarosite (h^+) are strong oxidizing agents capable of reacting with water to generate hydroxyl radicals (˙OH) *via* the reaction shown in eqn (2). The high oxidative power of these holes facilitates the efficient conversion of water into ˙OH radical, which plays a key role in the degradation of organic pollutants such as RhB through direct oxidation (eqn. (4)).

Given that direct electron transfer from the CB of jarosite to O_2 is unlikely, the production of $^{\cdot}O_2$ radicals could involve an alternative mechanism through Fe^{3+}-mediated electron transfer since Jarosite contains iron in both Fe^{3+} and Fe^{2+} oxidation states. Photogenerated electrons may reduce Fe^{3+} to Fe^{2+} (eqn (3a)), and the Fe^{2+} can subsequently reduce O_2 to $^{\cdot}O_2$ *via* an indirect process (eqn (3b)).

Through a series of reactions, superoxide radicals ($^{\cdot}O_2$) further convert into hydrogen peroxide (H_2O_2) and subsequently generate hydroxyl radicals (˙OH) (eqn (5) and (6)). These ROSs play a crucial role in breaking down organic contaminants, ultimately leading to their degradation into harmless products (eqn (7)).

This proposed mechanism aligns with trapping test results, confirming the enhanced photocatalytic efficiency of jarosite

$$\text{Jarosite} + h\nu \rightarrow e^- + h^+ \quad (1)$$

$$h^+ + H_2O \rightarrow {}^{\cdot}OH \quad (2)$$

$$e^- + Fe^{3+} \rightarrow Fe^{2+} \quad (3a)$$

$$Fe^{2+} + O_2 \rightarrow Fe^{3+} + {}^{\cdot}O_2 \quad (3b)$$

$$h^+ + \text{RhB} \rightarrow \text{degradation products} \quad (4)$$

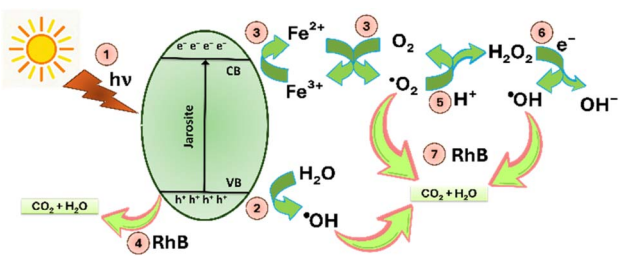

Fig. 6 Photocatalytic mechanism of Jarosite for RhB degradation under sunlight irradiation.

$$2H^+ + 2\ {}^{\cdot}O_2 \rightarrow O_2 + H_2O_2 \quad (5)$$

$$H_2O_2 + e \rightarrow {}^{\cdot}OH + OH^- \quad (6)$$

$$^{\cdot}O_2/H_2O_2/{}^{\cdot}OH + \text{RhB} \rightarrow \text{degradation products} \quad (7)$$

Conclusions

In this study, we developed a simple and environmentally friendly route for synthesizing magnetite and jarosite nanoparticles using banana peel extract as both a natural stabilizing agent and potassium source. This approach eliminates the need for hazardous chemicals and supports the principles of green chemistry and sustainability. Jarosite outperformed magnetite in photocatalytic degradation of RhB, achieving >99% removal within 30 minutes with a rate constant nearly twice that of magnetite. The jarosite catalyst maintained >94% of its activity over five consecutive reuse cycles and achieved 92% TOC removal after 60 minutes, confirming its excellent stability and ability to mineralize organic contaminants.

Optimization studies identified that a banana extract prepared at a 1 : 20 solid-to-liquid ratio and 30 minutes of microwave heating produced jarosite with the highest photocatalytic efficiency. Mechanistic investigations, supported by photoluminescence analysis and scavenger tests, revealed that hydroxyl radicals were the predominant reactive species generated through a photo-Fenton-like process facilitated by efficient charge separation.

Overall, this work highlights the dual benefit of agricultural waste valorisation and effective pollutant removal, providing a scalable, low-cost pathway to produce high-performance photocatalysts. The strategy can be extended to other biomass sources and pollutants, supporting sustainable wastewater treatment and contributing to global efforts toward clean water and responsible consumption as outlined in the UN Sustainable Development Goals.

Author contributions

Hui Wen Neo: conceptualization, investigation, data curation, formal analysis, visualization, writing – original draft. Eslam M. Hamed: methodology, supervision, validation, writing – review & editing. Fun Man Fung: resources, project administration, funding acquisition, supervision, writing – review & editing. Sam F. Y. Li: conceptualization, funding acquisition, project administration, supervision, writing – review & editing.

Conflicts of interest

There are no conflicts to declare.

Data availability

All datasets generated and analyzed during this study are available upon request.

Supplementary information: general materials, sample characterization data, and figures (pdf). Impression of the synthesis process of magnetite. (A) mixing Fe(II) and Fe(III) ions. (B) adjusting the pH to 11. (C) the washed precipitate is strongly attached to the magnet. Impression of the synthesis process of jarosite. (A) Microwave Fe(III) ions and banana peels extract under reflux. (B) The formed precipitate. (C) The brownish-black precipitate after centrifugation. Photocatalytic properties (band gap, rate constant, degradation efficiency) of jarosite and magnetite. See DOI: **https://doi.org/10.1039/d5su00731c**.

Acknowledgements

Eslam M. Hamed is funded by a full scholarship from the Ministry of Higher Education of the Arab Republic of Egypt. This research collaboration was supported by a University College Dublin grant awarded to F. M. Fung.

Notes and references

1 B. Pegu and S. Konwer, *Graphene 2D Mater.*, 2023, **8**, 121–133.
2 L. Wang, X. Qiang, L. Huan, X. Wang, W. Gu, J. Niu, Q. Fan and G. Wang, *New J. Chem.*, 2025, **49**, 1725–1735.
3 P. Kumar, S. Ashique, H. Sharma, S. Yasmin, A. Islam, S. Mandal, B. H. J. Gowda, M. Khalid, M. Y. Ansari, M. Singh, I. Ehsan, T. Taj and F. Taghizadeh-Hesary, *Bioorg. Chem.*, 2025, **157**, 108305.
4 P. Cui, C. Liu, X. Su, Q. Yang, L. Ge, M. Huang, F. Dang, T. Wu and Y. Wang, *Environ. Sci. Technol.*, 2022, **56**, 8034–8042.
5 U. O. Aigbe and O. A. Osibote, *J. Hazard. Mater. Adv.*, 2024, **13**, 100401.
6 J. Zweigle, B. Bugsel, C. Capitain and C. Zwiener, *Environ. Sci. Technol.*, 2022, **56**, 15728–15736.
7 T. Yang, M. Chen, J. Li, Z. Feng, S. Zou, S. Mao, Z. Tian and H. Zhao, *Environ. Sci. Technol.*, 2025, **59**, 8155–8166.
8 R. Azam, K. Malik, T. Sultana, F. Arooj and A. Kazmi, *Physiol. Mol. Plant Pathol.*, 2025, **136**, 102586.
9 D. Hatinoglu, J. Lee, J. Fortner and O. Apul, *Environ. Sci. Technol.*, 2023, **57**, 12191–12200.
10 K. M. Mahnoor, A. Kazmi, T. Sultana, N. I. Raja, Y. Bibi, M. Abbas, I. A. Badruddin, M. M. Ali and M. N. Bashir, *Heliyon*, 2025, **11**, e41654.
11 O. P. Bolade, A. B. Williams and N. U. Benson, *Environ. Nanotechnol. Monit. Manag.*, 2020, **13**, 100279.
12 J. León-Flores, J. L. Pérez-Mazariego, M. Marquina, R. Gómez, R. Escamilla, S. Tehuacanero-Cuapa, C. Reyes-Damián and J. Arenas-Alatorre, *J. Cluster Sci.*, 2023, **34**, 2381–2395.
13 L. Soltys, O. Olkhovyy, T. Tatarchuk and M. Naushad, *Magnetochemistry*, 2021, **7**, 145.
14 W. M. Hikal, H. A. H. Said-Al Ahl, A. Bratovcic, K. G. Tkachenko, J. Sharifi-Rad, M. Kačániová, M. Elhourri and M. Atanassova, *Evid. base Compl. Alternative Med.*, 2022, **2022**, 7616452.
15 J. Scaria, M. Pédrot, L. Fablet, T. Yomogida, T. T. Nguyen, Y. Sivry, C. Catrouillet, A. E. Pradas Del Real, F. Choueikani, D. Vantelon, A. Dia, A. Groleau and R. Marsac, *Environ. Sci. Technol.*, 2025, **59**, 5747–5755.
16 A. Nunez Garcia, M. Lee, L. Ding, X. Liang, C. Wang, F. He and D. M. O'Carroll, *Environ. Sci. Technol.*, 2025, **59**, 3172–3182.
17 T. A. Aragaw, F. M. Bogale and B. A. Aragaw, *J. Saudi Chem. Soc.*, 2021, **25**, 101280.
18 X. Zhang, D. Wei, H. Zhang, Y. He, S. Zhang, J. Dai and X. Wen, *Biochem. Eng. J.*, 2022, **180**, 108371.
19 A. Mohamed, R. R. Atta, A. A. Kotp, F. I. Abo El-Ela, H. Abd El-Raheem, A. Farghali, D. H. M. Alkhalifah, W. N. Hozzein and R. Mahmoud, *Sci. Rep.*, 2023, **13**, 7227.
20 H. H. Mohamed, D. H. A. Besisa, N. Besisa and T. E. Youssef, *Mater. Sci. Eng., B*, 2023, **296**, 116634.
21 I. Rabani, C. Bathula, R. Zafar, M. Shoaib Tahir, Y.-J. Park, H.-S. Kim, M. Naushad and Y.-S. Seo, *J. Colloid Interface Sci.*, 2022, **608**, 2347–2357.
22 E. U. Ikhuoria, I. E. Uwidia, R. O. Okojie, I. H. Ifijen, I. D. Chikaodili and A. Fatiqin, *J. Multidiscip. Appl. Nat. Sci.*, 2023, **4**, 108–119.
23 C. Harmansah, M. Karatay Kutman and F. Z. Biber Muftuler, *Measurement*, 2022, **204**, 112081.
24 T. D. Sowers, M. D. Blackmon, S. E. Bone, A. M. Kirby, M. L. Jerden, M. R. Noerpel, K. G. Scheckel and K. D. Bradham, *Environ. Sci. Technol.*, 2022, **56**, 15718–15727.
25 C. Yu, A. Johnson, A. Karlsson, R. Chernikov, V. Sjöberg, Z. Song, M. Dopson and M. E. Åström, *Environ. Sci. Technol.*, 2024, **58**, 18324–18334.
26 V. Kumar Singh, S. Manna, J. Kumar Biswas and A. Pugazhendhi, *J. Environ. Manage.*, 2023, **343**, 118221.
27 S. Ray, L. Daudi, H. Yadav and G. D. Ransinchung, *J. Clean. Prod.*, 2020, **272**, 122546.
28 S. Yan, L. Zhan, X. Meng, D. Wang, X. Wang, G. Zheng, J. Lu and L. Zhou, *Sep. Purif. Technol.*, 2021, **274**, 118991.
29 Y. Dong, Z. Wang, X. Yang, M. Zhu, R. Chen, B. Lu and H. Liu, *RSC Adv.*, 2016, **6**, 102972–102978.
30 M. Cruells and A. Roca, *Metals*, 2022, **12**, 802.
31 B. O. Oyeyinka and A. J. Afolayan, *Plants*, 2019, **8**, 598.
32 K. H. Hama Aziz, F. S. Mustafa, M. A. H. Karim and S. Hama, *Mater. Adv.*, 2025, **6**, 3433–3454.
33 K. H. Hama Aziz, F. S. Mustafa, M. A. H. Karim and S. Hama, *J. Environ. Manage.*, 2025, **390**, 126245.
34 H. R. Ahmed, K. H. Hama Aziz, N. N. M. Agha, F. S. Mustafa and S. J. Hinder, *RSC Adv.*, 2023, **13**, 26252–26266.
35 M. A. H. Karim and K. H. Hama Aziz, *J. Water Proc. Eng.*, 2025, **75**, 108014.
36 F. S. Mustafa and K. H. Hama Aziz, *Process Saf. Environ. Prot.*, 2023, **170**, 436–448.
37 A. Ahmadian, S. Ahmadi and B. A. Goharrizi, *Int. J. Environ. Sci. Technol.*, 2023, **20**, 6433–6448.
38 S. Labib, S. Abdelaal, A. M. Abdelhady and E. K. Elmaghraby, *Mater. Chem. Phys.*, 2020, **256**, 123654.
39 P. Kubelka, *J. Opt. Soc. Am.*, 1948, **38**, 448–457.
40 K. H. Hama Aziz, H. Miessner, S. Mueller, A. Mahyar, D. Kalass, D. Moeller, I. Khorshid and M. A. M. Rashid, *J. Hazard. Mater.*, 2018, **343**, 107–115.

41 M. Idrees, Z. U. Haq Khan, S. Sabahat, J. Sun, N. S. Shah and J. Iqbal, *J. Mol. Liq.*, 2025, **424**, 127115.
42 S. K. Giri and N. N. Das, *Desalination Water Treat.*, 2016, **57**, 900–907.
43 Y. Liu, C. Liao, L. Liu, X. Zhu, Z. Chen, D. Ren, T. Yang and Y. Sun, *Miner. Eng.*, 2024, **219**, 109083.
44 D. Dinesh, A. Dinesh, S. Maria Packiam, L. Srimathi Priya, S. Pon Sakthi Sri, M. George, K. Radhakrishnan, A. Manikandan, M. Santhamoorthy, N. S. Topare, A. Khan, N. Azum, K. A. Alzahrani and H. M. Marwani, *Inorg. Chem. Commun.*, 2024, **169**, 113129.
45 T. B. Mbuyazi and P. A. Ajibade, *Int. J. Mol. Sci.*, 2024, **25**, 7876.
46 M. K. Jaiswal, S. Deka, T. Kalita, D. J. Kalita and B. Choudhury, *ACS Sustain. Chem. Eng.*, 2024, **12**, 14670–14683.